ORIGINAL ARTICLE

Coherent structures in turbulent mixed convection flows through channels with differentially heated walls

Claus Wagner[1,2] | Tim Wetzel[2]

[1]Institute of Thermodynamics and Fluid Mechanics, Technische Universität Ilmenau, Thüringen, Germany

[2]Institute of Aerodynamics and Flow Technology, German Aerospace Center, Niedersachsen, Germany

Correspondence
Claus Wagner, Center for International Researchers, Technische Universität Ilmenau, Helmholtzring 1, 98693 Ilmenau, Germany. Email: claus.wagner@tu-ilmenau.de

Abstract

The occurrence and shape of turbulent structures in mixed convection flows through a differently heated vertical channel are investigated in terms of thermally induced attenuation and amplification of turbulent velocity, pressure, and temperature fluctuations using direct numerical simulations. It is shown that the wall-normal momentum transport is decreased and increased near the heated and cooled wall, respectively, and that this leads to a reduced and elevated production of turbulent velocity fluctuations in the streamwise velocity component in the aiding and opposing flow, respectively. The corresponding flow structures are smoother, faster and warmer in the aiding flow and aligned along the main flow, while the colder structures in the opposing flow are more frayed and less directed. The warmer flow structures in the aiding flow are overall more stable than the colder structures in the opposing flow. Besides, the study reveals that the position of the maximum temperature fluctuations moves toward the heated wall, so that the sweeps produced at the two walls are affected differently by the former. As a consequence, the distance and time period over which the fluctuations develop in the aiding flow are shorter than in the opposing flow. It is further shown that vortex structures oriented in the streamwise direction usually arise with an offset to the right or left above a sweep or an ejection, whereby the decreasing values of the correlation coefficients with increasing Grashof number indicate a weakening of the vortex structures. Since none of the evaluated vortex criteria, that is, the distributions of the vorticity, λ_2- value or Rortex-value correlate well with the evaluated minima of the pressure fluctuations, they do not allow a clear identification of the vortex structures. Finally, analyzing the budget of the turbulent kinetic energy it is confirmed that the velocity fluctuations are only indirectly influenced by the buoyancy force. Thus, the attenuation and

amplification of the turbulent velocity fluctuations is reflected in the reduction and exaggeration of the Reynolds shear stresses in the aiding and opposing flow, respectively.

1 | INTRODUCTION

Mixed convection flows, that is, forced flows influenced by temperature induced buoyancy forces, play a major role in nature and technology. In engineering, this type of flow often occurs in heated or cooled pipes, channels and ducts of heat exchangers, air conditioning systems, solar thermal collectors, and cooling systems of reactors and electronic components. Due to the outstanding importance of mixed convection flows, one can find a large number of studies in the literature dealing with mixed convection flow in pipes and channels in a wide variety of fields and using different methods. For example, Zamora and Kaiser [37] simulate laminar flows in a collector and storage wall for passive use of solar energy, a so-called Trombe wall, solving the Reynolds-averaged Navier–Stokes equations (RANS). In doing so, they are investigating how the design of the inlet and outlet ducts can be optimized in terms of heat transport and flow routing. Also Boulemtafes-Boukadoum and Benzaoui [3] use RANS simulations with different turbulence models to predict the mixed convection flow in a solar thermal collector. They vary the roughness of the absorber to analyze the effects of its transverse placement on the change of heat transfer and thus optimize the heat transfer. Other studies are concerned with the air-conditioning of rooms, such as Taghinia et al. [32], who predict natural and mixed convection flows in a room to evaluate the reliability of turbulence models commonly used in RANS-simulations and hybrid RANS-LES.

The flow simulations performed for the use cases presented above show that the challenges in predicting mixed convection flows through vertical pipes, channels or ducts are particularly significant. This is likely related to the fact that the understanding of the energy transfer between turbulent flow structures of different size as well as the development of turbulence models is first and foremost based on studies of purely forced flows. For this reason, more fundamental studies are devoted either to the selection and adaptation of turbulence models to the case of vertical mixed convection flows, such as Kim et al. [16], who compare results from RANS simulations of turbulent flow in a vertical pipe with strong wall heating with different turbulence models and results from direct numerical simulation (DNS), or to the objective of the present work, that is, to improve the understanding of the attenuation and amplification of the coherent flow structures in turbulent mixed convection flow in vertical channels. Since the attenuation may eventually lead to laminarization, selective heating of the walls could also be used to control a turbulent flow. This could be significant in light of the study by Kühnen et al. [19], who show in experiments and numerical simulations of isothermal turbulent pipe flows that by selectively and suddenly increasing the wall normal gradient of the mean velocity at a constant mean volume flow rate at a defined location in the pipe, turbulent velocity fluctuations are strongly attenuated until the flow eventually laminarizes.

1.1 | Coherent flow structures in purely forced shear flows

Although, coherent structures of turbulent shear flows are investigated for many years, they are not clearly defined. Pope [28], for example, describes coherent flow structures generally as temporally and spatially limited regions in the fluid, such as the streaks, sweeps, and ejections, but also eddies and inner shear layers, which can be identified as coherent fluctuating regions by means of flow visualization. Along these lines, Kline et al. [18] show with hydrogen bubble and color injection visualizations of velocity fluctuations in a turbulent flow over a plate that meandering flow structures (streaks) over 1000 wall units in length and with transversal spacing between 67 and 312 wall units exist in the viscous sublayer. These streaks grow in a region located about 15 wall units away from the plate and are transported away by the mean flow. In the process, they lift up from the plate by the lift-up mechanism and, triggered by secondary instabilities, start to oscillate in a region with a wall distance between 8 and 12 wall units. The oscillations intensify with increasing wall

distance until the streaks burst in a region with a wall distance between 10 and 30 to subsequently leave the buffer layer as an ejection. This process provides the turbulent momentum exchange between the viscous sublayer and outer flow layers and contributes significantly to the generation of the Reynolds shear stresses. Kline et al. [18] refer to the streaks as quasi-coherent structures with inflated or depressed momentum, which arise from vortex-like structures near the wall and are characterized by their coherent vorticity. Hussain [9] argues that only fluid regions with coherent vorticity can be considered turbulent flow structures in the strict sense. This definition follows from conservation of energy, since only structures defined in this way exhibit some degree of self-preservation. In his paper on the unambiguous definition of vortex structures, Haller [7] explains a procedure that determines vortex structures as coherent Lagrangian structures by means of their Lyapunov exponents, independent of the reference frame. He also discusses the differences to other vortex definitions such as the Q- or λ_2-criteria. These two criteria are based on invariants of velocity gradients and interpret local pressure minima as vortex centers, respectively. However, since the velocity gradients used can also be due to shear layers, most vortex criteria are not invariably reliable in identifying coherent vortex structures. What is indisputable, apart from any disagreement on their definition, is that the patterns formed by the structures can be used to assign order to the inherently chaotic nature of turbulent flows, to explain mechanisms of turbulence generation and maintenance, and to modify them to control turbulence.

To look more closely at the momentum transport organized in the flow structures, Swearingen and Blackwelder [31] create counter-rotating vortices in the streamwise direction of the flow across a flat plate using a Görtler instability mechanism. They find that fluid with low momentum is transported away from the wall in the slow streaks between vortices, while fluid with high momentum originating from the bulk approaches the wall where it is organized in fast streaks. In isothermal turbulent channel and pipe flows, these streaks have lengths of up to 1000 wall units at a spacing of $\lambda^+ \approx 100$ wall units, which was confirmed, for example, by Kim et. al. [16], Lyons et al. [23], and Kasagi et al. [13] in DNSs at Reynolds numbers of $Re_\tau = 180$ ([15]) and $Re_\tau = 150$ ([13,23]), respectively, for the channel flow and for example, by Wagner and Friedrich [33] for a pipe flow at $Re_\tau = 180$.

These and other findings from experimental and numerical studies on the turbulence structure in wall-bounded shear flows are summarized in a review article by Jiménez [12]. In the latter, the structures in the buffer layer are treated separately from those in the logarithmic layer, since the prevailing structures have different temporal and spatial correlation measures. Additionally, it is shown that the streaks in the buffer layer scale in internal units (wall inits), that they have constant dimensions in wall units regardless of the Reynolds number, and that they are very subject to the influence of local shear. In contrast, the larger structures in the logarithmic layer scale in external units and are less affected by the much lower local shear further away from the wall.

1.2 | Buoyancy effect in vertical mixed convection flows

Studies focusing on the origin and evolution of coherent flow structures are mostly concerned with the simpler, purely forced flows in ducts, channels, and pipes. If buoyancy forces additionally play a supporting role in turbulent vertical mixed convection flows, there is often more interest in reducing heat transfer and turbulent velocity fluctuations due to thermal buoyancy effects. Metais and Eckert [25], for example, collected the results of papers published before the year 1964 studying turbulent flows in horizontal and vertical pipes with heat transfer. Regarding vertical mixed convection flows, they show that the turbulent velocity variations and heat transfer strongly depend on the degree of heating. They divide the flow cases into forced, mixed, and free convection as a function of Rayleigh (Ra) and Reynolds (Re) numbers and introduce the distinction between opposing and aiding vertical flows. Motivated by the observation that the latter can laminarize under certain circumstances, Steiner [30] conducts vertical pipe flow experiments. He shows that the mean flow profile is deformed due to buoyancy effects, derives the necessary conditions for flow relaminarization and makes the buoyancy-induced acceleration in the center of the pipe responsible for the laminarization which takes place near the wall where it leads to a reduction of the Nusselt number Nu.

In the experimental study of heated vertical pipe flow of Narasimha and Sreenivasan [26], Steiner's results are confirmed. They further show that the turbulent velocity fluctuations are damped due to the influence of the buoyancy forces on the mean flow until finally relaminarization sets in. This effect which is also well-known from stably stratified flows, where rising fluid loses kinetic energy while working against the gravitational force, is also addressed in Jackson and Hall [10] who compile findings on heat transport in mixed convection of fluids at supercritical pressure, showing that the decrease in heat transport in aiding vertical pipe flows has often been attributed to stratification effects. Considering experimental results from the literature, they further postulate for vertical pipe flows that buoyancy effects significantly

influence the turbulent fluctuations and heat transport for $Gr/Re^{2.7} > 10^{-5}$ (here Gr denotes the Grashof number). Launder [21] also comes to a similar conclusion in a review article, in which he also postulates that the buoyancy force in vertical flows only exerts an indirect influence. He makes mainly the pressure reflections at impermeable walls responsible for the observed attenuation and amplification of the turbulent velocity fluctuations.

In another review article, Petukhov et al. [27] summarize the results from theoretical and experimental studies of heat transport in mixed convection flows. Their analysis of integral quantities focuses on the characteristics of heat transport in laminar and turbulent, horizontal and vertical boundary layer, pipe, and channel flows. They show that buoyancy forces in mixed convection flows affect turbulent fluctuations and heat transport through two mechanisms. For this they take up the distinction of the indirect and direct effect of buoyancy forces by Launder [20] and postulate that buoyancy forces in the so-called structural effect directly affect the turbulent energy balance by changing the correlation between velocity and temperature whereas the external or indirect effect, which is dominant in vertical flows, is due to the turbulent fluctuations acting on the flow as a whole through the inhomogeneous distribution of the buoyancy force.

Performing DNS, Bae et al. [2] predict flows in vertical pipes with heated walls for a compressible fluid and study the statistical changes in the fluid for varying Gr and Re. Their analysis of statistical moments reveals a strong buoyancy effect on the turbulent velocity fluctuations in that they are attenuated at high heating powers. They attribute this effect to the large thermally induced density changes of the fluid. Similarly, they are able to show that this causes the turbulent heat flux to change more at low than at high heating powers.

Also based on results from numerical flow simulations, You et al. [36] investigate the aiding and opposing airflows in vertical pipes for different ratios of Gr/Re. Here, the obtained mean axial velocity profiles in the aiding flow exhibit an M-shape and increased values in the opposing flow. Moreover, they are able to show that the axial velocity fluctuations and Reynolds shear stresses decrease for increasing ratios of Gr/Re in the aiding flow and, vice versa, in the opposing flow. They observe that the streaks of turbulent velocity fluctuations and the structures of temperature fluctuations are very similar in the opposing flow near the wall while they are more different in the aiding flow. Using DNS results of incompressible vertical pipe flows, He et al. [8] study the effects of changing the shape factor and the intensity of the volume force, showing which specific combinations of these effects contribute to the relaminarization of the flow.

In contrast, Wetzel and Wagner [34], Kasagi and Nishimura [14], and Fabregat et al. [5] perform DNS of the flow in a vertical channel with a heated and a cooled wall. Consistently, these studies show that the coherent structures become longer and shorter with increasing Grashof number near the heated and cooled walls, respectively, while their convection velocities generally decrease. Moreover, the study of Wetzel and Wagner [34] reveals that the decrease and increase of the Reynolds shear stresses in the aiding and opposing flow, respectively, are the main causes for the attenuation and amplification of the turbulent velocity fluctuations on these respective channel sides.

Anyway, the general aim of several experimental studies of vertical mixed convection flows, for example by Aicher et al. [1], Celataa et al [4], Liu et al. [22], and Kirillov [17], is to improve the prediction of the heat transfer coefficient or the Nusselt number on the basis of measured data. However, these studies do not provide an improved physical understanding of the processes dominating in the aiding and opposing flow. Further, the literature also shows that laminar and turbulent vertical mixed convection flow behave very similar in terms of mean flow velocity, whereas the heat transfer characteristics differ significantly. While a faster aiding flow improves the heat transfer between the wall and the fluid in the laminar case, turbulent velocity fluctuations are damped reducing the mixing and, consequently, the heat transfer in the case of a turbulent flow. This phenomenon is often described by the indirect effect according to Launder [20] and Petukhov et al. [27] which is confirmed and supplemented by the results and physical details in Wetzel [35] and Wetzel and Wagner [34], which are reviewed and extended in the present article.

2 | COMPUTATIONAL DETAILS OF THE CHANNEL FLOW SIMULATIONS

The dimensionless, incompressible Navier–Stokes equations obtained under the Boussinesq approximation are solved to predict the turbulent flow of a Newtonian fluid of density $\hat{\rho}$ through the vertical channel with height $\hat{\delta}$, length $\hat{L} = 2.5\pi\hat{\delta}$ and width $\hat{W} = \pi\hat{\delta}$ (dimensional quantities are denoted by $\hat{\ }$) using periodic boundary conditions in axial and transversal direction, x_1 and x_2, respectively. Further, impermeability and no slip boundary conditions are imposed at the side walls held at the constant dimensionless temperatures $\theta_h = 0.5$ and $\theta_c = -0.5$, respectively. The dimensions of the channel domain are the same as the ones used by Wetzel and Wagner [34] and Kasagi and Nishimura [14]. The dimensionless velocity components are defined as $u_i = \hat{u}_i/\hat{u}_b$ with the bulk velocity $\hat{u}_b$, the Cartesian coordinates $x_i = \hat{x}_i/\hat{\delta}$, the pressure

TABLE 1 Dimensionless numbers, grid resolution and time step realized in the direct numerical simulation

Gr	$Re_{\tau,h}$	Re_τ^*	$Re_{\tau,c}$	Δ_1^*	Δ_2^*	$\Delta_{3,min}^*$	$\Delta_{3,max}^*$	$\overline{h}^*$	Δ_t^*
0	—	284.02	—	4.36	3.48	0.16	3.62	3.80	$8.42 \cdot 10^{-6}$
$6.4 \cdot 10^5$	299.10	288.58	277.67	4.42	3.54	0.16	3.66	3.85	$8.55 \cdot 10^{-6}$
$9.5 \cdot 10^5$	307.85	291.46	274.1	4.48	3.59	0.16	3.70	3.90	$8.63 \cdot 10^{-6}$
$1.6 \cdot 10^6$	331.41	301.21	267.63	4.62	3.70	0.18	3.84	4.10	$8.93 \cdot 10^{-6}$

$p = \hat{p}/(\hat{\rho}\hat{u}_b^2)$ and the temperature $\theta = (\hat{T} - \hat{T}_0)/\Delta\hat{T}$ with the mean temperature $\hat{T}_0 = (\hat{T}_h + \hat{T}_c)/2$ and the temperature difference $\Delta\hat{T} = \hat{T}_h - \hat{T}_c$ between the walls.

The discretized Navier–Stokes equations are solved on staggered grids using a fourth order accurate finite volume method together with a second-order accurate explicit Euler-leapfrog time integration scheme. A summary of the dimensionless numbers $Pr = \hat{v}/\hat{\kappa} = 0.71$, $Re_b = (\hat{u}_b\hat{\delta})/\hat{v} = 4328$ and $Gr = (\hat{g}\hat{\beta}\Delta\hat{T}\hat{\delta}^3)/\hat{v}^2$ with the kinematic viscosity $\hat{v}$, the thermal conductivity $\hat{\kappa}$ and the thermal expansion coefficient $\hat{\beta}$ realized in the below discussed DNS as well as the resulting global and local friction Reynolds numbers at the heated and cooled walls, Re_τ^* (* denotes with averaged wall shear stress velocity normalized quantity), $Re_{\tau,h}$ and $Re_{\tau,c}$, respectively, are listed in Table 1 together with grid widths $\Delta_1^*, \Delta_2^*, \Delta_3^*$ in the three Cartesian directions x_1, x_2, x_3 and the time step Δ_t^*.

In Table 1 $\overline{h}^* = \sqrt[3]{\Delta_1^* \cdot \Delta_2^* \cdot \Delta_{3,max}^*}$ denotes the realized mean grid widths which are all below the grid with $h^+ = 4.31$ needed to resolve Kolmogorov scale in a DNS. The flow is driven against the gravitational acceleration $\hat{g}$ by a mean pressure gradient $\langle p \rangle$ which is adapted to realize a prescribed Re_b. For more details on the numerical method and the performed simulation the reader is referred to Wetzel and Wagner [34].

3 | MEAN AND RMS FLUCTUATING VELOCITIES AND TEMPERATURES

Figure 1 shows the mean velocity profiles for the channel halves at the heated and cooled wall in red and blue, respectively, for the three considered Grashof numbers $Gr = 6.4 \cdot 10^5$ (dotted lines), $Gr = 9.5 \cdot 10^5$ (dashed lines) and $Gr = 1.6 \cdot 10^6$ (dashed-dotted lines) in comparison with the mean velocity profile of the isothermal channel flow ($Gr = 0$) in black (solid line). The evaluation of statistical mean values started $50u_\tau/\delta$ dimensionless time units after the heating and cooling was turned on in a DNS of fully developed isothermal channel flow for $Re_b = 4328$. At this time the flow through the differentially heated channel reached a statistically independent equilibrium state since the wall shear stresses were fluctuating around constant mean wall shear stresses. Subsequently, statistical averaging in the periodic directions and in time, denoted by $\langle(.)\rangle$, was performed for at least $60u_\tau/\delta$ dimensionless time units. The resulting profiles of the mean axial velocity component in Figure 1 are asymmetric due to the different wall temperatures which lead to different wall shear stresses. At Grashof numbers $Gr = 6.4 \cdot 10^5$, $Gr = 9.5 \cdot 10^5$, and $Gr = 1.6 \cdot 10^6$, respectively, the mean wall shear stresses $4.7 \cdot 10^{-3}, 5.1 \cdot 10^{-3}$, and $5.9 \cdot 10^{-3}$, respectively, are obtained at the heated wall and $4.1 \cdot 10^{-3}, 4.0 \cdot 10^{-3}$, and $3.9 \cdot 10^{-3}$, respectively, at the cooled wall. These values are higher for the aiding flow as the mean wall shear stress $4.3 \cdot 10^{-3}$ of the isothermal channel flow at $Re_b = 4328$ and $Gr = 0$ and, vice versa, lower for the opposing flow. In order to allow a direct comparison of the velocity profiles plotted over the dimensionless wall distance in local wall units, the curves shown in Figure 1 are normalized by the local friction velocities.

In the aiding flow, that is, on the heated channel side, the fluid is flowing faster as the heating, that is, Gr number, increases in contrast to mean velocities of the opposing flow at the cooled channel side, which decrease with increasing Grashof number. Thus, the thermal buoyancy forces cause an acceleration or deceleration of the fluid in the aiding or opposing flow, respectively, on a time-average basis. Additionally, Wetzel and Wagner [34] and Kasagi and Nishimura [14] showed that the logarithmic range of velocity profiles in the aiding flow becomes smaller with increasing Grashof number, since the maximum of the mean velocity moves toward the heated wall while in the opposing flow it propagates in the center of the channel. Since the maximum $\partial\langle u_1 \rangle/\partial x_3 = 0$, that is, the location where the mean shear rate disappears, increases with increasing Grashof number $Gr = 6.4 \cdot 10^5$, $Gr = 9.5 \cdot 10^5$, and $Gr = 1.6 \cdot 10^6$, respectively, the mean shear rates increase directly at the heated wall by 5.3%, 11.6%, and 21.0%, respectively, and conversely decrease at the cooled wall by 8.3%, 11.6%, and 19.9%, respectively. These changes in mean shear rates behave similarly to the changes of the wall shear stresses normalized by Reynolds number Re_τ discussed above.
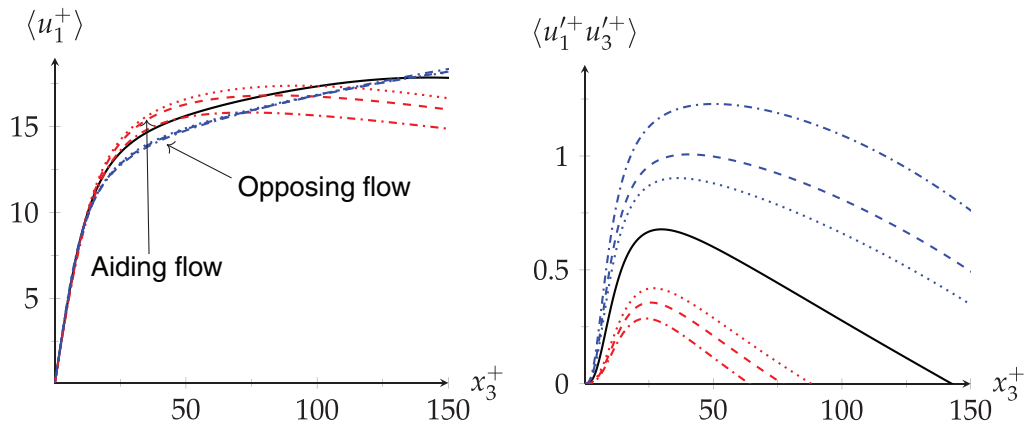
FIGURE 1 Profiles of mean axial velocity (left) and Reynolds shear stresses (right) normalized by the local friction velocity of the warm (red) or blue (cold) wall. Solid: $Gr = 0$, dotted: $Gr = 6.4 \cdot 10^5$, dashed: $Gr = 9.5 \cdot 10^5$, dashed-dotted: $Gr = 1.6 \cdot 10^6$
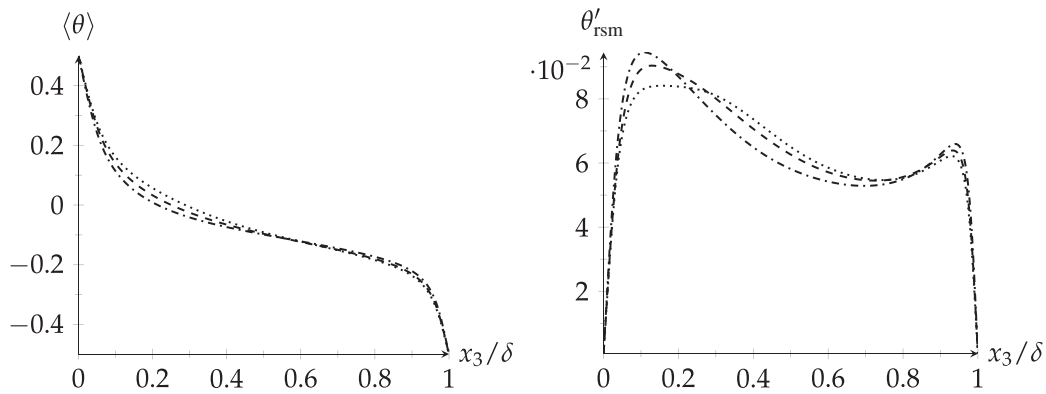
FIGURE 2 Profiles of averaged temperature (left) and rms temperature fluctuations (right) as functions of wall distance in outer units. Dotted: $Gr = 6.4 \cdot 10^5$, dashed: $Gr = 9.5 \cdot 10^5$, dashed-dotted: $Gr = 1.6 \cdot 10^6$

The Reynolds shear stresses plotted in Figure 1 (right) also show that the values in the aiding flow decrease with increasing Grashof number and increase in the opposing flow. Compared to the isothermal channel flow, the maxima and zero crossings also shift toward the heated wall in the aiding flow and away from the cooled wall in the opposing flow. Since the values of the Reynolds' shear stresses can be regarded as a statistical measure of the strength of the sweeps and ejections, this also shows that the wall-normal momentum transport in these coherent structures is damped in the aiding flow and enhanced in the opposing flow. Furthermore, it was shown in Wetzel and Wagner [34] that the indirect buoyancy effect postulated by Petukhov et al. [27] causes the asymmetry of the turbulent velocity fluctuations.

The profiles of the mean temperature in Figure 2 (left) reflect the expected behavior with a steady decline between the maximum at the heated wall and minimum at the cooled wall. Only in the bulk region between $0.1 < x_3/\delta < 0.5$ leads the increasing buoyancy, that is, Grashof number, to a slight decrease in the mean temperature. More surprising is the behavior of the maxima of the rms temperature fluctuations in Figure 2 (right) which are higher in the aiding than in the opposing flow for two reasons and behave differently as the rms velocity fluctuations in the axial and wall-normal directions, whose maximum values decrease in the aiding and increase in the opposing flow with increasing Grashof number. On the one hand, higher temperature fluctuations are produced in the aiding flow due to the steeper temperature gradient, and on the other hand, the position of the maximum temperature fluctuations moves toward the heated wall, so that the sweeps produced at the two walls are affected differently by the former. In the aiding flow, the distance and time period over which the fluctuations develop are shorter than in the opposing flow. This additionally contributes to the fact that turbulent mixing is reduced in the aiding flow, so that the compensation of the temperature fluctuations is also less pronounced.

4 | INSTANTANEOUS FLUCTUATING FLOW STRUCTURES

In order to give an impression of the influence of the buoyancy forces on the development of the sweeps and ejections and the thereby induced near-wall streaky structures, which are known to play a significant role in the wall-normal momentum transport in isothermal channel and pipe flow, three-dimensional (3D) isocontour surfaces of the velocity and temperature fluctuations, u' and Θ', predicted for the Grashof number $Gr = 9.5 \cdot 10^5$ are shown in Figure 3. For this purpose, the mean velocity and temperature fields, $\langle u_i \rangle$ and $\langle \Theta \rangle$, plotted in Figures 1 and 2, respectively, were subtracted from two instantaneous axial velocity and temperature fields, u and Θ, respectively. In Figure 3, the 0.9-, 0.7-, 0.5-, and 0.4-fold values of the minimum and maximum velocity and temperature fluctuations are visualized and colored accordingly. In order to distinguish the isocontour surfaces lying within each other, their opacity was set to 40%. To compare the structures in the aiding and opposing flow, the flow field was split into two subdomains by dividing the complete flow domain along the wall-parallel plane $z/\hat{\delta} = 0.3$, which is the wall-normal distance of the maximum of the mean velocity profile. For plotting purposes, the viewing directions in these subdomains representing the aiding and opposing flow are directed toward the heated and cooled walls, respectively. The isocontour surfaces of the velocity fluctuations shown in Figure 3 each include 60% of the fastest and slowest velocity values, which can be interpreted as high and low momentum regions. They form the streaks well-known from the literature on isothermal wall-bounded flows, for example, Kline et al. [18].

Comparison of the isocontours in the aiding flow (left) and the opposing flow (right) shows that there are fewer and smoother streaks in the aiding flow than in the opposing flow. Similarly, the isocontours of the temperature fluctuations Θ' reflect smoother warm structures in the aiding flow aligned along the main flow, while the structures near the cold wall representing the opposing flow appear more frayed and less directed. It is also known that the structures shown in Figures 3 and 4 interact with streaks and temperature structures in the boundary layer near the wall, which are oriented in the flow direction. However, it is not yet clear whether the streaks arise from the vortex structures and are therefore equally abundant, or whether and where they dominate. The latter would suggest that the vortex structures arise from the streaks only when conditions are favorable. It is therefore obvious to visualize these vortex structures in the instantaneous flow fields and to compare the vortex structures obtained in the aiding and opposing flow. For this purpose, isocontour surfaces of the magnitudes of vorticity ($|\omega'^+| = 0.55$), of the λ_2-criterion ($|\lambda_2| = -0.03$), and of the Rortex criterion ($|R| = 0.15$) are analyzed below.
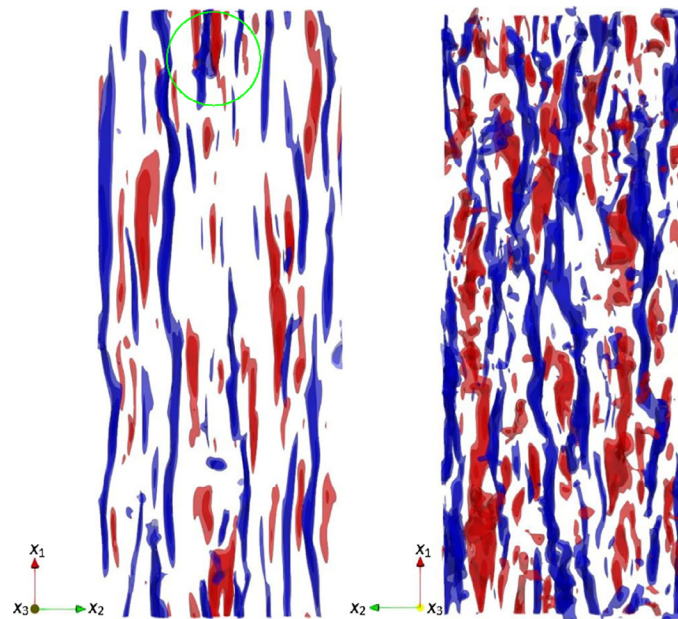
FIGURE 3 Three-dimensional plot of isocontour surfaces of the 0.9-, 0.7-, 0.5-, and 0.4-fold values of the minimum (blue) and maximum values (red) of the the streamwise velocity fluctuations u'_1 obtained for $Gr = 9.5 \cdot 10^5$ closed to the heated wall (left) and the cooled wall (right). In order to distinguish overlapping isocontour surfaces their opacity was set to 40 % The green outline marks a prominent area in the flow for later comparison with vortex criteria
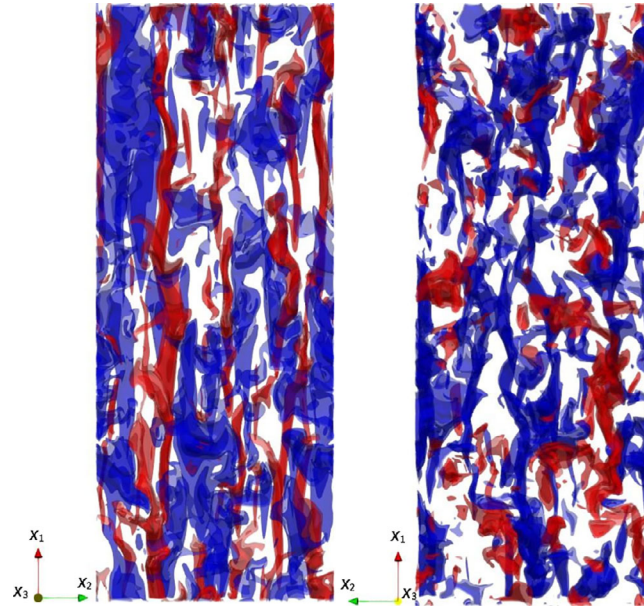
FIGURE 4 Three-dimensional plot of isocontour surfaces of the 0.9-, 0.7-, 0.5-, and 0.4-fold values of the minimum (blue) and maximum values (red) of the temperature fluctuations obtained for $Gr = 9.5 \cdot 10^5$ closed to the heated wall (left) and the cooled wall (right). In order to distinguish overlapping isocontour surfaces their opacity was set to 40%

5 | VORTEX IDENTIFICATION

It is well-known that the velocity gradient tensor $L_{ij} = \partial u_i / \partial x_j = s_{ij} + \Omega_{ij}$ can be decomposed into the shear rate tensor $s_{ij} = 1/2(\partial u_i / \partial x_j + \partial u_j / \partial x_i)$ and the rotation rate tensor $\Omega_{ij} = 1/2(\partial u_i / \partial x_j - \partial u_j / \partial x_i)$. From Ω_{ij}, the vorticity vector $\omega_i = -\epsilon_{ijk}\Omega_{jk}$, with ϵ_{ijk} the Levi - Civita - symbol is obtained which measures the local rotation of the fluid. Isosurfaces of $|\omega_i|$ indicate fluid regions with coherent rotational strength, which can be interpreted as an indicator for the presence of vortex structures. However, due to the formulation of the vorticity vector, it can also respond in regions of high shear rates without vortex structures. Therefore, the vorticity vector is not an unambiguous criterion for indicating vortex structures.

The λ_2 criterion presented by Jeong et al. [11] is based on the insight that there must be a local pressure minimum at the center of a vortex. To determine the pressure minima, the eigenvalues of the symmetric part of the Navier–Stokes equations

$$\Omega_{ik}\Omega_{kj} + s_{ik}s_{kj} = -\frac{\partial^2 p_{ij}}{\partial x_i \partial x_j}, \tag{1}$$

which neglects transient, viscous, and thermal effects. This expression has only real eigenvalues λ_i, so for $\lambda_2 < 0$ and $\lambda_1 \geq \lambda_2 \geq \lambda_3$ there are two negative eigenvalues and thus, a local pressure minimum. Since the isocontour surfaces of a fixed negative value of the λ_2 field enclose local pressure minima, they consequently indicate potential locations of vortex structures.

Finally, since the velocity gradient tensor L_{ij}-based invariants are susceptible to shear influence, Liu et al. [21] developed the so-called Rortex method for visualizing vortex structures. The latter is based on the Rortex vector R_i, which results from a transformation of the velocity gradient tensor and can be considered as a measure of pure rotational motion. Isocontour surfaces of $|R|$, like vorticity, indicate contiguous regions of similar rotational strength and provide at least mathematical confidence that this is pure rotation in the fluid.

The structures shown above are contiguous areas with stronger velocity or temperature fluctuations. In order to decide whether and, if so, how these structures are related to the well-known vortex structures in the wall boundary layer of the turbulent channel flow fields of fluctuating vorticity, of λ_2-values and of $|R|$-values are compared in Figures 5–8. In order to be able to compare the appearance of the streaky structures in a plane of one selected instantaneous flow field, a cluster of streaky structure which is visible in all plots shown in Figures 5–7 is highlighted with a green circle.
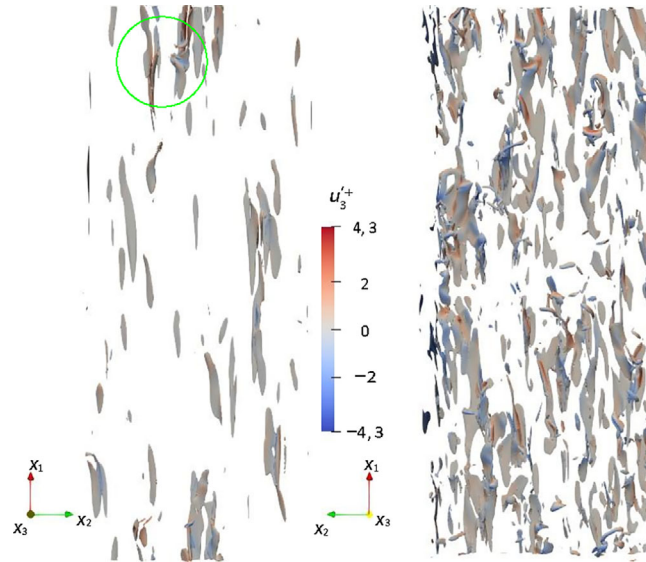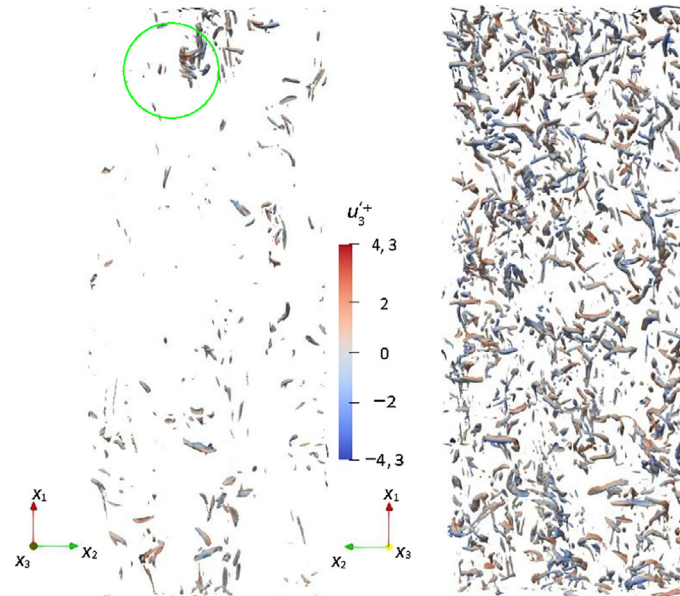
FIGURE 5 Isocontour surfaces of the vorticity for $|\omega'^+| = 0.55$ in the aiding (left) and opposing flow (right). The color coding of the isocontours corresponds to the wall-normal velocity component. The green circle marks a highlighted region with selected structures
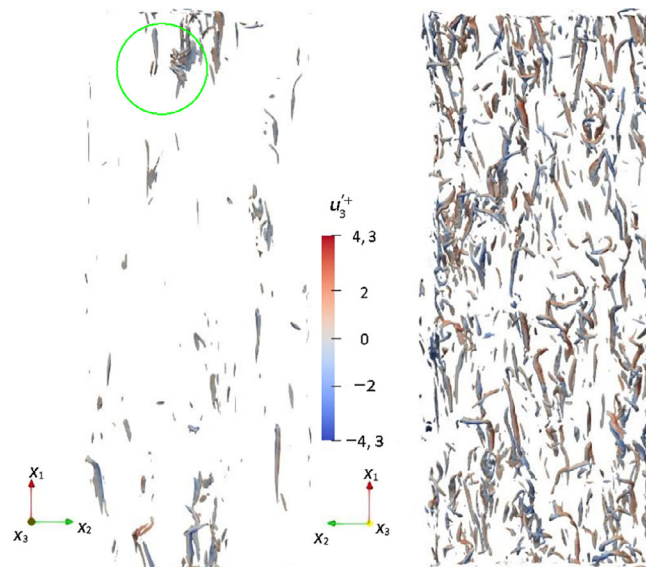
FIGURE 6 Isocontour surfaces of the λ_2 criterion for $|\lambda_2| = -0.03$ in the aiding (left) and opposing flow (right). The color coding of the isocontours corresponds to the wall-normal velocity component. The green circle marks a highlighted region with selected structures

Looking first at the isocontours of the vorticity fluctuations $|\omega'^+| = 0.55$ shown in Figure 5, elongated regions of coherent vorticity fluctuations are visible in both, the aiding and the opposing flow. The comparison with Figure 3 reveals that they are partially bounding the streaks. Further, the above-discussed attenuation leads to less and smoother vorticity structures in the aiding than in the opposing flow, which is consistent with the appearance of the streaks in Figure 3 in these flow regions. A closer look on the wall-normal velocities of these different vortex structures reveals that not all regions of coherent vorticity necessarily correspond to vortex structures due to the following: In the area outlined in green for example, the fluctuations are distributed in such a way that no clear vortex structure can be identified. In comparison, the isocontours for $\lambda_2 = -0.03$-value in Figure 6 are organized in narrower and shorter regions on both channel sides. In the aiding flow (Figure 6 left), they are predominantly oriented in the flow direction, while in the opposing flow, some structures in Figure 6 right also point in the cross-flow direction. Considering their wall normal velocities, the isocontours indicate the presence of vortex structures, although the isocontours of λ_2 in the marked region

FIGURE 7 Isocontour surfaces of the Rortex criterion for $|R| = 0.15$ in the aiding (left) and the opposing (right) flow. The color coding of the isocontours corresponds to the wall-normal velocity component. The green circle marks a highlights region with selected structures

reflect a collection of undirected structures. This is even more evident in the isocontours for the Rortex values $|R| = 0.15$ in Figure 7, which on the one hand reflect values that are of the same order of magnitude as the λ_2 values, but on the other hand are predominantly oriented in the cross-flow direction.

Considering that the Rortex criterion, according to the developers Gao and Liu [6], is less responsive to shear fluctuations than the λ_2 criterion, we can assume that the $|R|$-fields are more likely to reflect the existence of vortex structures.

Since none of the above considered vortex criteria provides clear evidence for the existence of vortex structures in the plane with a wall spacing $y^+ = 15$, where the streaky structures are known to cluster, the question arises whether they can be found elsewhere and how they are related to the streaky structures. To answer this Figure 8B–D shows an exemplary comparison in a cross-section perpendicular to the flow direction through the area marked in green, where the isocontours surfaces of $|\omega'^+| = 0.55$ in Figure 8B, of $|\lambda_2| = -0.03$ in Figure 8C, and of $|R| = 0.15$ in Figure 8D are colored red and blue with the values of the velocity fluctuations in the wall-normal direction and are superimposed on the isocontours of the local pressure fluctuations p'^+. In addition, in Figure 8A, the vectors of velocity fluctuations in the cross-flow and wall-normal directions are superimposed on the local pressure fluctuations p'^+. In the center of Figure 8A, a pair of fast and slow streaks can be seen with a vortex-like structure above them around a local pressure minimum on the left and right sides, respectively. The comparison with the isocontours of the vorticity fluctuations in Figure 8B at this location reveals that they completely fill the region between the fast and slow streaks, suggesting that the vortex fluctuations indicate shear between the streaks. In addition, none of the $|\lambda_2|$ isocontours in Figure 8B corresponds to a local pressure minimum, although the λ_2 criterion should respond exactly there based on its formulation. Furthermore, for all criteria shown in Figure 8B–D, there is no clear correlation between their isocontours and the occurrence of pressure minima, so that the vortex criteria presented here do not allow a clear identification of vortex structures, although there is a high chance that the latter develop in the neighborhood of a streaky structure.
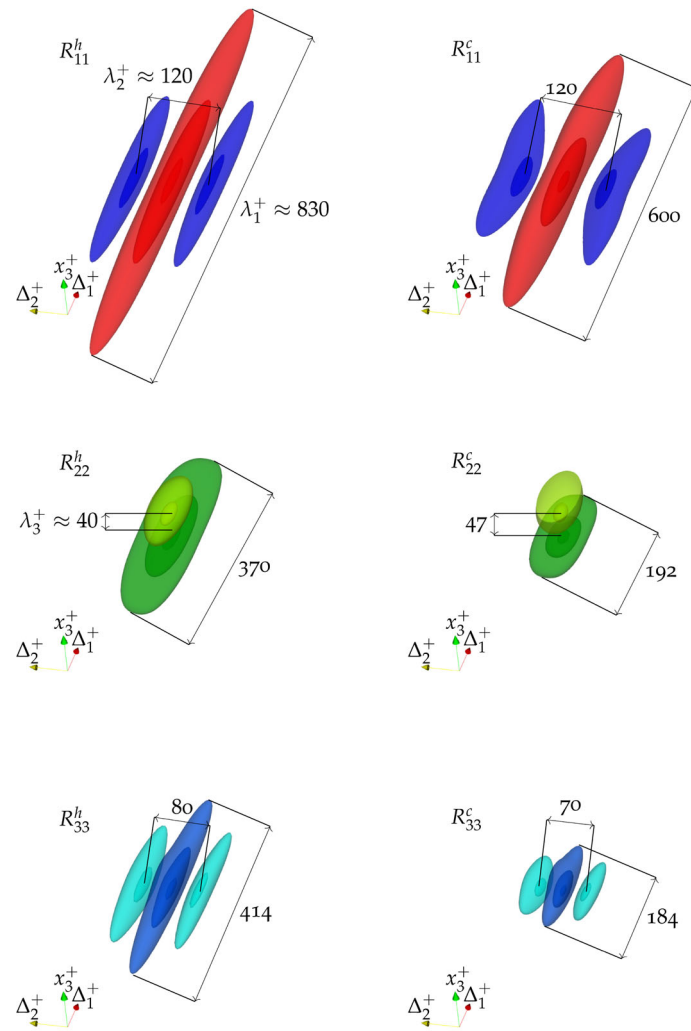
6 | CORRELATION FUNCTIONS

The statistical analogon to the instantaneous flow structures presented in Figure 3 are the 3D distributions of the correlation coefficients of the velocity fluctuations $R_{ii}(\Delta_1^+, \Delta_2^+, \Delta_3^+, x_{3,\text{ref}}^+)$ which depend on the separations Δ_i^+ in x_i-directions in wall units in relation to the reference position $x_{3,\text{ref}}^+$ and result from averaging in the periodic x_1- and x_2-directions and in time. For more details on the above presented correlation functions and their evaluation for channel flows the reader is referred to Sillero et al. [29].
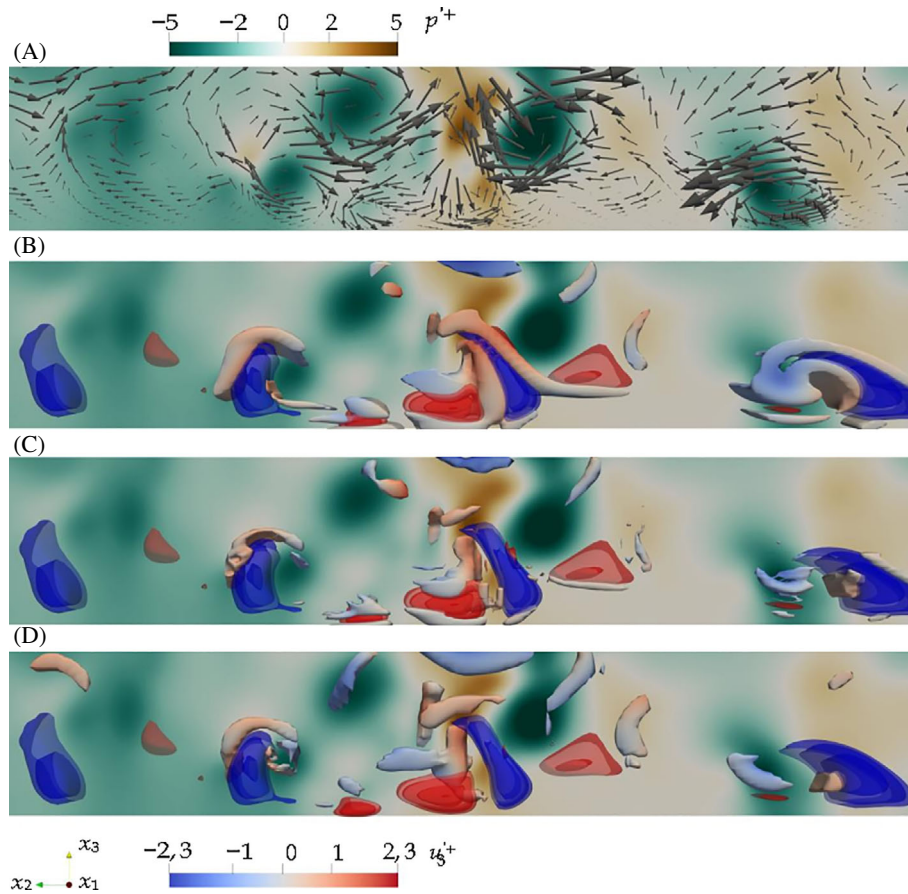
FIGURE 8 (A) Isocontours of the pressure fluctuations p'^{+} together with vectors of the fluctuating velocity field, (B) isocontour surfaces of the vorticity fluctuations, (C) of the λ_2 criterion, (D) and the Rortex criterion. In (B)–(D) all isocontours are colored according to the wall-normal velocity fluctuations. The three-dimensional isocontours of the fast streaks are colored red, while the slow streaks are colored blue

To identify the influence of the buoyancy forces on the streaky structures in the near-wall flows for $Gr = 9.5 \cdot 10^5$, the 3D autocorrelation functions $R_{ii}(\Delta_1^+, \Delta_2^+, \Delta_3^+, x_3^+ = 15)$ of the three velocity components evaluated at a wall distance $x_3^+ = 15$ are presented in Figure 9, on the left for the aiding and on the right for the opposing flow. The isocontours in Figure 9 reflect 0.9- and 0.5-times the maximum and minimum values of the correlation function, respectively, with their opacity was set to 40% to make the inner contour surfaces visible. The plots illustrate the transversal spacing $\lambda^+ \approx 100$ between the minima and maxima of the correlation functions of the axial and wall-normal velocity fluctuations u_1' and u_3', respectively, well-known from isothermal turbulent channel flow, for both, the aiding and the opposing flow. In contrast, no transversal spacing is observed for the minima of the u_2' correlation function which is located farther away from the wall than the maximum. Obviously, the structures represented by the isosurfaces of the correlation function are longer in the aiding flow than in the opposing flow. Since the minima of the correlation coefficients in Figure 10 are smaller in the opposing flow than in the aiding flow, the observation from the instantaneous isosurfaces of the axial velocity fluctuations in Figure 3 that the smoother coherent regions of the fluctuation motion are overall more stable in the aiding flow is confirmed.

How these structures change with the Grashof number is additionally answered analysing the isocontour lines of the autocorrelation functions R_{11}, R_{22}, R_{33} in the cross-sectional plane of the Δ_2^+, x_3^+ plane for $\Delta_1^+ = 0$ in Figure 10 and in the Δ_1^+, x_3^+ plane for $\Delta_2^+ = 0$ in Figure 11 for $Gr = 6.4 \cdot 10^5$ (top), $Gr = 9.5 \cdot 10^5$ (middle), and $Gr = 1.6 \cdot 10^6$ (bottom). In the cross-section Δ_2^+, x_3^+, the correlation lengths in the wall-normal direction increase and decrease with increasing Grashof number in the aiding and opposing flow, respectively. Conversely, with increasing Grashof numbers the wall-normal extents of the regions of equal correlation coefficients of the u_2' and u_3' components increase in the aiding flow and decrease in the opposing flow. Moreover, the streaks reflected by R_{11} at $x_3^+ = 15$ project less far or farther into the channel center in the aiding and opposing flow, respectively, than for the corresponding isothermal flows (dashed lines). Moreover, the dimensions of the mean flow structures represented by R_{22}, R_{33} in the wall-normal direction show an opposite
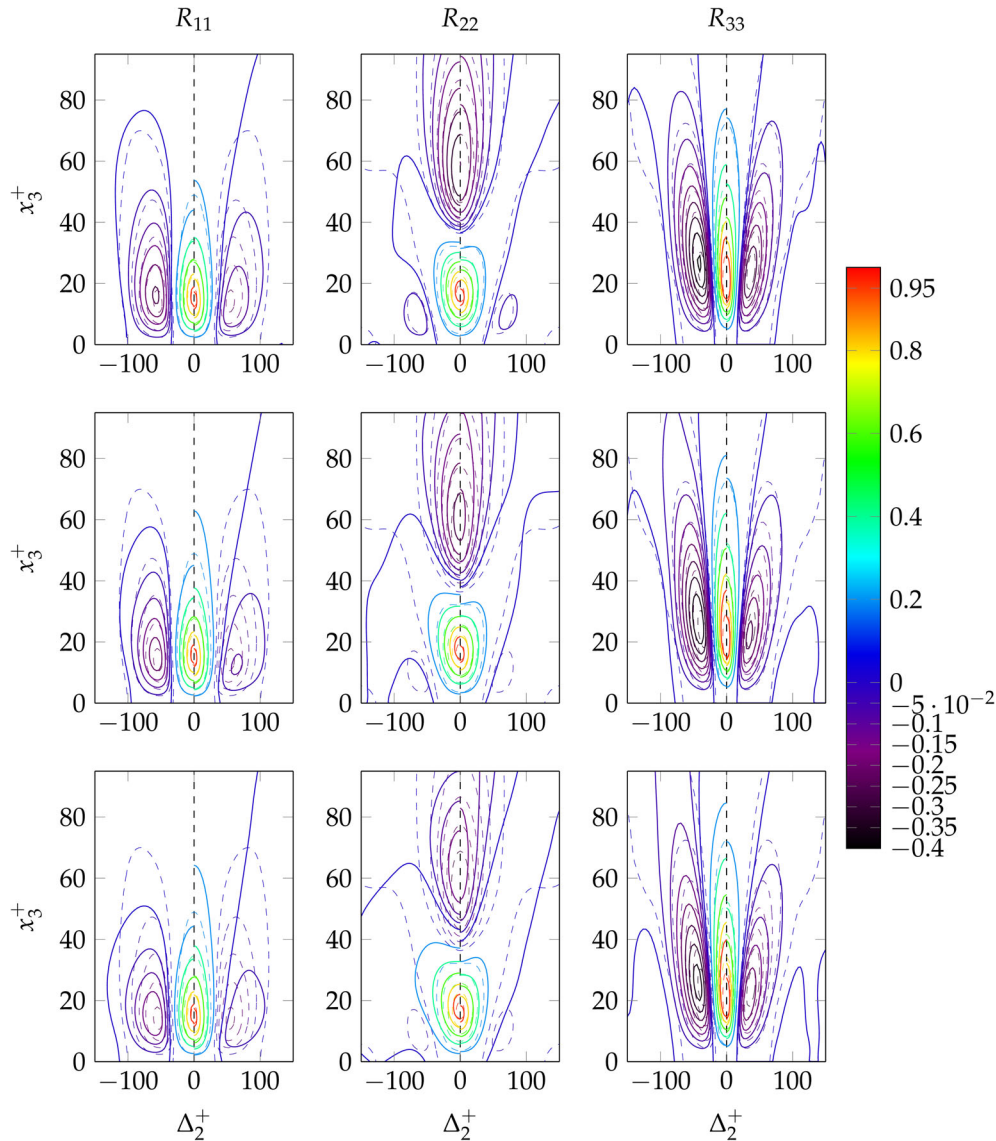
FIGURE 9 Isocontour surfaces of three-dimensional autocorrelation functions of velocity fluctuations in the flow, crossflow, and wall-normal directions (from top to bottom) in the aiding (left) and opposing flow (right) for $Gr = 9.5 \cdot 10^5$. Shown are isocontour surfaces for 0.9- and 0.5-times the maxima and minima values, and additionally for 0.2- times the maximum value. The length of the structures λ_1^+ in flow direction as well as the distance λ_2^+ and λ_3^+ in transversal and direction in wall-normal direction are also given

behavior with increasing Grashof number. In the aiding flow, the dimensions in wall-normal direction increase while they decrease in the opposing flow. Further, as discussed above, the distances between the minimum and maximum of R_{11} in the transversal direction can be regarded as half the width of the streaks. In isothermal channel flow, the width of the streaks equals 55.8 viscous length (or wall) units. In the investigated range of Grashof numbers, the streak width decreases by about 9% in the aiding flow, while it increases by about 18% in the opposing flow. Similarly, the structure widths increase by about 25% in the aiding flow and decrease by about 8.5% in the opposing flow when the correlation function of the wall-normal velocity component is considered. Regarding the lengths of the above discussed structures, the isocontours of the autocorrelation functions R_{ii} in the Δ_1^+, x_3^+ plane at $\Delta_2^+ = 0$ in Figure 11 reflect regions of positive correlation values of R_{11}, that is, the average lengths of the streaks, which are longer in the aiding flow for $Gr = 6.4 \cdot 10^5$ with $\lambda_1^+ \approx 500$ than for $Gr = 0$ with $\lambda_1^+ \approx 400$. This is also true for the correlation functions R_{22} and R_{33}, which are generally longer in the aiding flow for $Gr > 0$ than in the isothermal case and whose length increases with increasing Grashof number. In contrast, the lengths in the opposing flow decrease with the Grashof number.

In order to be able to interpret and analyze the transport processes in the correlation regions of the three velocity components shown above and to illustrate their interaction with the vortex structures typically occurring in wall-bounded flows, the positions of a sweep or an ejection are marked in color in the principle sketch in Figure 12A,B, respectively,
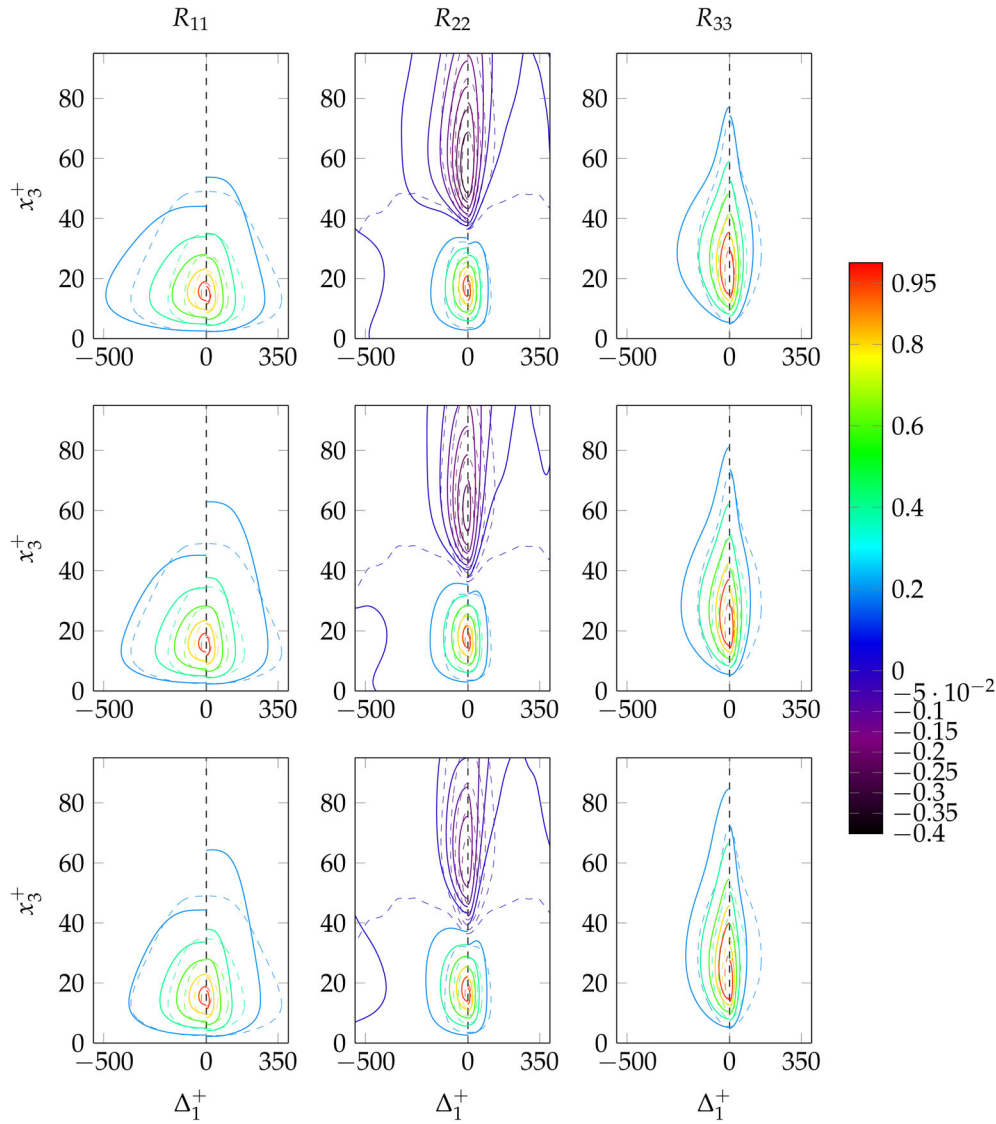
FIGURE 10 Isocontours of the three-dimensional autocorrelation functions $R_{ii}(\Delta_1^+ = 0, \Delta_2^+, x_3^+, x_3^{+,\text{ref}} = 15)$ in sectional planes for $Gr = 6.4 \cdot 10^5$ (top), $Gr = 9.5 \cdot 10^5$ (middle), and $Gr = 1.6 \cdot 10^6$ (bottom) of the three fluctuating velocity components $u_1'^+$ (left), $u_2'^+$ (middle), and $u_3'^+$ (right) shown in solid contour lines. The comparison case $Gr = 0$ is plotted as dashed contour lines. The left half of each figure $(\Delta_2^+ < 0)$ shows the correlation function in the aiding flow, the right half $(\Delta_2^+ > 0)$ that in the opposing flow

where the directions in which the fluid moves during a sweep or an ejection are indicated by additional arrows in areas with positive values of the correlation function. In addition, fluid in areas with negative values of the correlation function moves in the opposite direction as in areas with positive values. Furthermore, in both principle sketches the vortices are drawn which are compatible with the direction of fluid movements indicated by the arrows. Accordingly, a vortex structure directed in the direction of flow can occur on the right or left above a sweep and on the right or left above an ejection. The sketches in Figure 12A,B represent a sweep and an ejection, respectively, and the arrows in the dark-colored dots representing areas with positive values of the respective correlation function indicate the respective directions in which the fluid moves in a sweep or in an ejection.

Taking into account that the directions of fluid motion in areas with negative correlation values are in principle opposite to the directions in areas with positive correlation values, both sketches represent vortices that can result from the indicated fluid motions. Accordingly, in the case of a sweep (Figure 12 left), a vortex structure directed in streamwise direction can occur only to the right above a sweep and, in the case of an ejection (Figure 12 right), only to the left above the flow structures. However, since both sweeps and ejections are characterized only by the directions of u_1 and u_3, the

FIGURE 11 Isocontours of the three-dimensional autocorrelation functions $R_{ii}(\Delta_1^+, \Delta_2^+ = 0, x_3^+, x_3^{+,\text{ref}} = 15)$ in sectional planes for $Gr = 6.4 \cdot 10^5$ (top), $Gr = 9.5 \cdot 10^5$ (middle), and $Gr = 1.6 \cdot 10^6$ (bottom) of the three fluctuating velocity components $u_1'^+$ (left), $u_2'^+$ (middle), and $u_3'^+$ (right) shown in solid contour lines. The comparison case $Gr = 0$ is plotted as dashed contour lines. The left half of each figure ($\Delta_2^+ < 0$) shows the correlation function in the aiding flow, the right half ($\Delta_2^+ > 0$) that in the opposing flow

transverse direction of motion can be reversed, so that vortices can also occur on the other side above the regions with positive correlation values. Therefore, the correlation values in Figures 10 and 11, which decrease with increasing Grashof number, indicate a weakening of the vortex structures in the opposing flow.

7 | BUDGET OF THE TURBULENT KINETIC ENERGY

In order to analyze the energy transfer associated with the attenuation and amplification of the turbulent velocity fluctuations, the time- and space-averaged balance equations of the turbulent kinetic energy (tke) given by Mansour et al. [24], according to which the sum S_{tke} of the production term P_{tke}, the pressure diffusion term D_{tke}, the turbulent diffusion term T_{tke}, the viscous diffusion term V_{tke}, the dissipation term E_{tke}, and the buoyancy production term B_{tke} vanishes, are analyzed and discussed below for the case $Gr = 9.5 \cdot 10^5$. Since Kasagi and Nishimura [14] also evaluated the balance equation using their DNS data calculated with a spectral method for same Grashof number, their results are included for comparison. First of all, the good agreement with the balance terms of Kasagi and Nishimura [14] underlines the
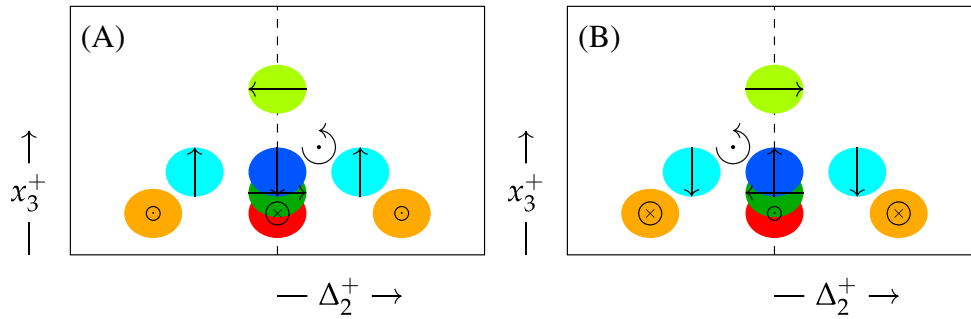
FIGURE 12 Principle sketch of the regions with positive and negative correlation coefficients R_{11}, R_{22}, and R_{33} in a cross-section. The assigned color corresponds to that in Figure 9. In addition, the flow directions of the fluid are shown exemplarily for a sweep in (A) and for an ejection in (B), respectively, together with the resulting vortices
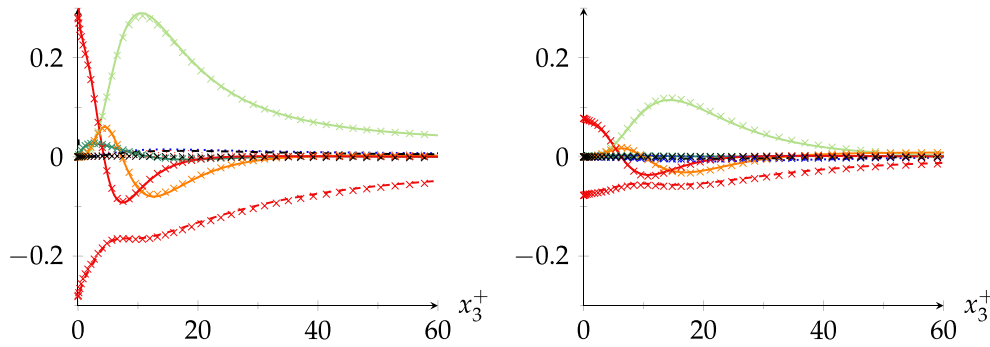
FIGURE 13 Profiles of the terms of the turbulent kinetic energy (tke) equation evaluated for $Gr = 9 \cdot 10^5$ in the aiding (left) and opposing (right) flow. Production term P_{tke}, buoyancy production term B_{tke}, pressure diffusion term D_{tke}, turbulent diffusion term T_{tke}, viscous diffusion term V_{tke}, viscous dissipation term E_{tke} and sum of all terms S_{tke}. Crosses represent comparative data from Kasagi and Nishimura [14]

reliability of the here presented DNS with the finite volume method. Second, the comparison of the different terms of the aiding (left) and opposing (right) flow qualitatively agrees with the profiles known from isothermal channel or pipe flows. From this it is concluded that the physical processes characteristic for isothermal turbulent channel flows are preserved even in the presence of differential heating of the vertically oriented channel walls, which, starting from both channel walls, divides the flow into the viscous sublayer for $x_3^+ < 5$, the buffer layer, in which the production term P_{tke} becomes maximum at $x_3^+ \approx 15$, and the fully turbulent (logarithmic) region $x_3^+ > 30$, above which the behavior of the turbulent energy fluctuations is largely determined by the balance between production and dissipation. The comparison between the aiding and opposing flows in Figure 13 left and right, respectively, further reveals that the absolute values of all terms are significantly lower in the aiding flow than in the opposing flow. It is also interesting to note that the values of the buoyancy production term B_{tke}, which represent the direct influence of the buoyancy force on the turbulent kinetic energy, are at least one order of magnitude lower than the values of the dominant terms. This underlines that the direct influence of the buoyancy force is small. Taking into account, that the reduction and exaggeration of the Reynolds shear stresses in the aiding and opposing flow, respectively, are the main causes for the respective attenuation and amplification of the turbulent velocity fluctuations (see Wetzel and Wagner [34]) the budget of the turbulent kinetic energy confirms that the velocity fluctuations are only indirectly influenced by the buoyancy force.

8 | CONCLUSIONS

DNSs of turbulent mixed convection flow through a differentially heated vertical channel are conducted with a fourth-order accurate finite volume method for the Prandtl number $Pr = 0.71$, the bulk Reynolds number $Re_b = 4328$ and four Grashof numbers $Gr = 0, 6.4 \cdot 10^5, 9.5 \cdot 10^5, 1.6 \cdot 10^6$. Instantaneous flow field snapshots, first- and second-order

moments, budget of the turbulent kinetic energy equations, visualizations of vortex criteria and 3D distributions of the autocorrelation coefficients reveal that the turbulent velocity fluctuations are attenuated in the aiding flow close to the heated wall and are enhanced in the opposing flow near the cooled wall. In contrast, temperature fluctuations are attenuated in the opposing flow and enhanced in the aiding flow. The instantaneous fluctuating velocity and temperature fields shown for the aiding and opposing flow, differ significantly in the shape and size of the turbulent structures and they are smoother in the aiding flow than in the opposing flow. In this sense, the mean velocity and temperature fields reflect a faster flow near the heated wall and a slower flow near the cooled wall. In addition, the mean temperature profile is shifted toward the heated wall. Due to the change in mean velocities, the local friction Reynolds number is higher in the aiding flow and lower in the opposing flow. Moreover, the friction Reynolds numbers increase in the aiding flow with increasing Grashof numbers and decrease correspondingly in the opposing flow. In the second-order statistical moments of the turbulent velocity and pressure fluctuations (see also Wetzel and Wagner [34]), an increase and decrease in the opposing and aiding flow, respectively, is evident. At first glance, these effects appear counterintuitive because with a higher local friction Reynolds number in the aiding flow, one would classically expect higher values of the turbulent velocity and pressure fluctuations and correspondingly lower values in the opposing flow. On the other hand, the rms temperature fluctuations show an opposite picture with stronger fluctuations in the aiding flow and weaker fluctuations in the opposing flow.

In contrast to the common assumption in the literature that the production of turbulent velocity fluctuations responds to buoyancy-induced changes in the mean shear rate, the evaluation of the balance equation of the turbulent kinetic energy underlines that in this case the indirect buoyancy effect is responsible for attenuation and amplification of the turbulent velocity fluctuations. Since the shear rate has little effect on the production term in the balance equations of the Reynolds stresses as pointed out in Wetzel and Wagner [34] it is concluded that the decrease in the production rate of turbulent fluctuation energy in the aiding flow and its increase in the opposing flow results from the change in Reynolds shear stresses, which is viewed as the statistical footprint of momentum transport in the streamwise and wall-normal directions and are related to sweeps and ejections through large-scale flow structures. Since turbulent kinetic energy is primarily produced in the axial velocity component and then redistributed to the other two components, Reynolds shear stresses are of particular importance in the redistribution to the wall-normal velocity component. By analyzing the redistribution process of turbulent fluctuation energy using the pressure-shear correlation, it it shown in [34] that the relative velocity between streaks in the vicinity of the walls, influences the redistribution significantly. This relative velocity is in turn influenced by their respective temperatures, as warm structures are accelerated and cold structures are decelerated by the buoyancy forces. Streaks arising in the aiding flow from ejections carry fluid with higher temperature than streaks arising there from sweeps, so that the relative velocity between them is reduced in the aiding flow. Vice versa, the relative velocity between the streaks increases in the opposing flow. As a result, lower local shear fluctuations occur in the aiding flow than in the opposing flow, which, in combination with the reduced and increased pressure fluctuations, directly affects the redistribution of turbulent fluctuation energy into the wall-normal velocity component. The previously described reduction in Reynolds shear stresses in the aiding flow is therefore a direct consequence of the reduced redistribution of turbulent kinetic energy into the wall-normal velocity component and, as a feedback effect, also leads to reduced production of turbulent kinetic energy. Vice versa, the increased redistribution of turbulent kinetic energy in the opposing flow leads to an increase in Reynolds shear stresses and thus also to an increase in the production of turbulent kinetic energy. In addition, the dimensions and distances of the turbulent flow structures were determined by forming the 3D distributions of the autocorrelation coefficients which provide contiguous regions with similar momentum. The visualizations of these 3D distributions show that the turbulent flow structures in the aiding flow are longer than in the corresponding isothermal flow, while the structures in the opposing flow are shorter. In contrast, the width of the structures remains nearly constant for all flow cases considered and is not affected by the buoyancy forces. Applying different vortex criteria on the aiding and opposing flow, the different intensities of the turbulent fluctuations in both regions was obvious. However, none of the considered criteria showed a clear correlation between their isocontours and the occurrence of pressure minima. Thus, the vorticity, λ_2 and Rortex-based criteria presented did not allow a clear identification of vortex structures although visualizations of the velocity vector and pressure fields in a cross-section provided evidence for the existence of these vortex structures. Finally, the comparison of the correlation functions reveals for the investigated range of Grashof numbers, that, compared to the streak width in the isothermal channel flow, the width of the streaks decreases by about 9% in the aiding flow and increases by about 18% in the opposing flow. Similarly, the structure width increases by about 25% in the aiding flow and decreases by about 8.5% in the opposing flow when the correlation function of the wall-normal velocity component is considered. Additionally, it is shown that the streaks are generally longer in the aiding flow for $Gr > 0$ than in the isothermal case and that these lengths increase with increasing Grashof number. In contrast, the lengths in the opposing flow decrease with the Grashof number.

The results discussed above on coherent structures in differentially heated channel flows are the basis for future research in the field of selective attenuation of turbulent flows by differentially heated pipes, where attenuation of turbulent fluctuations may eventually lead to laminarization, using selective heating of the walls to control a turbulent pipe flow. This may be possible in light of the study by Kühnen et al. [19], who show in experiments and numerical simulations of isothermal turbulent pipe flows that by selectively and suddenly increasing the wall normal gradient of the mean velocity at a constant mean volumetric flow rate at a defined location in the pipe, turbulent velocity fluctuations are strongly attenuated until the flow eventually laminarizes.

ACKNOWLEDGMENT

REFERENCES
[1] T. Aicher and H. Martin, New correlations for mixed turbulent natural and forced convection heat transfer in vertical tubes, Int. J. Heat Mass Transf. **40** (1997), no. 15, 3617–3626.

[2] J. H. Bae, J. Y. Yoo, H. Choi, and D. M. McEligot, Effects of large density variation on strongly heated internal air flows, Phys. Fluids **18** (2006), no. 7, 1–25.

[3] A. Boulemtafes-Boukadoum and A. Benzaoui, CFD based analysis of heat transfer enhancement in solar air heater provided with transverse rectangular ribs, Energy Proc. **50** (2014), 761–772.

[4] G. P. Celataa, F. Dannibale, A. Chiaradia, and M. Cumo, Upflow turbulent mixed convection heat transfer in vertical pipes, Int. J. Heat Mass Transf. **41** (1998), no. 24, 4037–4054.

[5] A. Fabregat, J. Pallares, A. Vernet, I. Cuesta, J. A. Ferre, and F. X. Grau, Identification of near-wall flow structures producing large wall transfer rates in turbulent mixed convection channel flow, Comput. Fluids **39** (2010), no. 1, 15–24.

[6] Y. Gao and C. Liu, Rortex and comparison with eigenvalue-based vortex identification criteria, Phys. Fluids **30** (2018), no. 8, 085107.

[7] G. Haller, An objective definition of a vortex, J. Fluid Mech. **525** (2005), 1–26.

[8] S. He, K. He, and M. Seddighi, Laminarisation of flow at low Reynolds number due to streamwise body force, J. Fluid Mech. **809** (2016), 31–71.

[9] F. Hussain, Coherent structures - reality and myth, Phys. Fluids **26** (1983), no. 10, 2816–2850.

[10] J. D. Jackson and W. B. Hall, "*Forced convection heat transfer to fluids at supercritical pressure*," *Turbulent forced convection in channels and bundles*, Vol **2**, McGraw-Hill, New York, NY, 1979, pp. 563–611.

[11] J. Jeong and F. Hussain, On the identification of a vortex, J. Fluid Mech. **285** (1995), 69–94.

[12] J. Jiménez, Near-wall turbulence, Phys. Fluids **25** (2013), no. 101302, 29.

[13] N. Kasagi, Y. Sumitani, Y. Suzuki, and O. Iida, Kinematics of the quasicoherent vortical structure in near-wall turbulence, Int. J. Heat Fluid Flow **16** (1995), 2–10.

[14] N. Kasagi and M. Nishimura, Direct numerical simulation of combined forced and natural turbulent convection in a vertical plane channel, Int. J. Heat Fluid Flow **18** (1997), 88–99.

[15] J. Kim, P. Moin, and R. D. Moser, Turbulence statistics in fully developed channel flow at low Reynolds number, J. Fluid Mech. **177** (1987), 133–166.

[16] W. S. Kim, S. He, and J. D. Jackson, Assessment by comparison with DNS data of turbulence models used in simulations of mixed convection, Int. J. Heat Mass Transf. **51** (2008), no. 5–6, 1293–1312.

[17] P. L. Kirillov, Heat transfer of turbulent flow. Part2: Velocity and temperature distributions, At. Energy **122** (2017), no. 4, 230–242.

[18] S. Kline, W. Reynolds, F. Schraub, and P. Runstadler, The structure of turbulent boundary layers, J. Fluid Mech. **30** (1967), no. 4, 741–773.

[19] J. Kühnen, D. Scarselli, M. Schaner, and B. Hof, Relaminarization by steady modification of the streamwise velocity profile in a pipe, Flow Turbul. Combust. **100** (2018), 919–943.

[20] B. E. Launder, "*Chapter second moment closure: Methodology and practice*," *Turbulence models and their applications*, Collection de la direction des etudes et recherches d'electricite de France, Vol **2**, P. Caseau, R. Dautray, and J. Lions (eds.), Eyrolles, Paris, 1984, pp. 5–147.

[21] C. Liu, Y. Gao, S. Tian, and X. Dong, Rortex-a new vortex vector definition and vorticity tensor and vector decompositions, Phys. Fluids **30** (2018), no. 3, 035103.

[22] D. Liu and H. Gu, Mixed convection heat transfer in a 5x5 rod bundles, Int. J. Heat Mass Transf. **113** (2017), 914–921.

[23] S. Lyons, T. Hanratty, and J. McLaughlin, Turbulence-producing eddies in the viscous wall region, Am. Inst. Chem. Eng. J. **35** (1989), no. 12, 1962–1974.

[24] N. N. Mansour, J. Kim, and P. Moin, Reynolds-stress and dissipation-rate budgets in a turbulent channel flow, J. Fluid Mech. **194** (1988), no. 1, 15–44.

[25] B. Metais and E. R. G. Eckert, Forced, mixed, and free convection regimes, J. Heat Transf. **86** (1964), no. 2, 295–296.

[26] R. Narasimha and K. R. Sreenivasan, Relaminarization of fluid flows, Adv. Appl. Mech. **19** (1979), 221–309.

[27] B. S. Petukhov, A. F. Polyakov, and B. E. Launder, *Heat transfer in turbulent mixed convection*, Hemisphere Publishing Corporation, New York, NY, 1988.

[28] S. Pope, *Turbulent flows*, Cambridge University Press, Cambridge, 2000.

[29] J. A. Sillero, J. Jimenez, and R. D. Moser, Two-point statistics for turbulent boundary layers and channels at Reynolds numbers up to d+ ≈ 2000, Phys. Fluids **26** (2014), no. 10, 105109.

[30] A. Steiner, On the reverse transition of a turbulent flow under the action of buoyancy forces, J. Fluid Mech. **47** (1971), no. 3, 503–512.

[31] J. D. Swearingen and R. F. Blackwelder, The growth and breakdown of streamwise vortices in the presence of a wall, J. Fluid Mech. **182** (1987), 255–290.

[32] J. Taghinia, M. Rahman, and T. Siikonen, Simulation of indoor airflow with RAST and SST-SAS models: A comparative study, Build. Simul. **8** (2015), no. 3, 297–306.

[33] C. Wagner and R. Friedrich, On the turbulence structure in solid and permeable pipes, Int. J. Heat Fluid Flow **19** (1998), 459–469.

[34] T. Wetzel and C. Wagner, Buoyancy-induced effects on large-scale motions in differentially heated vertical channel flows studied in direct numerical simulations, Int. J. Heat Fluid Flow **75** (2019), 14–26.

[35] T. Wetzel. *Analyse der Strukturbildung in turbulenten Mischkonvektionsströmungen auf Basis direkter numerischer simulationen*, PhD thesis, Technische Universität Ilmenau, 2020.

[36] J. You, J. Y. Yoo, and H. Choi, Direct numerical simulation of heated vertical air flows in fully developed turbulent mixed convection, Int. J. Heat Mass Transf. **46** (2003), no. 9, 1613–1627.

[37] B. Zamora and A. S. Kaiser, Thermal and dynamic optimization of the convective flow in Trombe Wall shaped channels by numerical investigation, J. Heat Mass Transf. **45** (2009), 1393–1407.